Systematic Study on Heat Transfer and Surface Hydrodynamics of a Vertical Heat Tube in a Fluidized Bed of FCC Particles

Xiuying Yao, Yongmin Zhang, and Chunxi Lu
State Key Laboratory of Heavy Oil Processing, China University of Petroleum, Beijing, 102249, P.R. China

Xiao Han
Pressure Pipeline Division, China Special Equipment Inspection and Research Institute, Beijing, 100029, P.R. China

DOI 10.1002/aic.14635

Bed-to-wall heat transfer properties of a vertical heat tube in a fluidized bed of fine fluid catalytic cracking (FCC) particles are measured systematically using a specially designed heat tube. Two important surface hydrodynamic parameters, i.e. the packet fraction (δ_{pa}) and mean packet residence time (τ_{pa}) based on the packet renewal theory, are determined by an optical fiber probe and a data processing method. The experimental results successfully reveal the axial and radial profiles of heat-transfer coefficient, the effects of superficial gas velocity, and static bed height on heat-transfer coefficient, most of which can be explained successfully by the measured τ_{pa}, an indicator of packet renewal frequency. τ_{pa} is found to play a more dominant role than δ_{pa} on bed-to-wall heat transfer. With a fitted correction factor, the modified Mickley and Fairbanks model is able to predict the heat-transfer coefficients with enough accuracy based on the determined packet parameters. © 2014 American Institute of Chemical Engineers *AIChE J*, 61: 68–83, 2015

Keywords: heat transfer, bed-to-wall, packet, surface hydrodynamics, fluidized bed, fluid catalytic cracking

Introduction

Fluidized beds are widely used in many industries, such as petroleum refining, chemical synthesis, food, pharmaceutical, power generation, and so forth, due to their excellent heat and mass transfer and violent solids mixing.[1,2] Fluidized-bed heat exchangers are often used in these fluidized processes for heat removal or addition. A typical case is the external catalyst cooler used in a fluid catalytic cracking (FCC) unit in petroleum refining industry,[3–5] which removes the superfluous heat exceeding the requirement by the endothermic cracking reactions and produces high-pressure stream by contacting fluidized catalyst particles with heat tubes. Despite of decades of usages in FCC units, tube leakage due to particle erosion, unexpected low cooling capacity due to bad bed-to-wall contact are frequently reported,[6–9] which all have negative influences on the long-term safe operation and the profitability of the FCC units. To obtain optimized designs of industrial external catalyst coolers, it is very necessary to understand the complex flow behavior of gas and particles and their effects on the heat transfer properties of an external catalyst cooler.

Generally, an external catalyst cooler is a gas-solids fluidized-bed heat exchanger with multiple vertical heat tubes. The dense-bed external catalyst coolers, which are mostly widely seen in FCC units, are usually operated in bubbling or turbulent flow regime. The heat tube often adopts a concentrically double-tube design.[4,8,10,11] Figure 1 shows a schematic of the design of a typical FCC external catalyst cooler widely used in China's refineries.[11,12] Hot particles enter into the cooler through the top entrance, then flow downward in the cooler and leave from the bottom exit. Cold water first flows downward through the small center tube and then turns upward to the annular flow area through the bottom exit of the center tube. During this process, the heat carried by the hot particles is transferred to the water through the tube wall by the vigorous contact between particles and the outer tube surfaces. As seen in Figure 1, every heat tube has independent water inlet and outlet for mixture. An advantage of this design is every heat tube can be shut down in case of leakage, but the whole external catalyst cooler can still be in service despite a part of loss in cooling capacity.

The heat transfer between fluidized particles and an immersed surface is often considered to have three addable mechanisms,[13] that is, radiation, gas convection and particle convection. The overall bed-to-wall heat-transfer coefficient in a dense fluidized bed is usually described as

$$h=h_{rad}+(1-\delta_{pa})h_g+\delta_{pa}h_p \tag{1}$$

Here δ_{pa} is the time fraction of packet when the heater surface is occupied by solids packets or contacted with the emulsion phase, $(1-\delta_{pa})h_g$ is the gas convection component during contact with lean bubble/void phase, $\delta_{pa}h_p$ is the

---

Correspondence concerning this article should be addressed to Y. Zhang at zym0876@gmail.com or C. Lu at lcx725@sina.com.

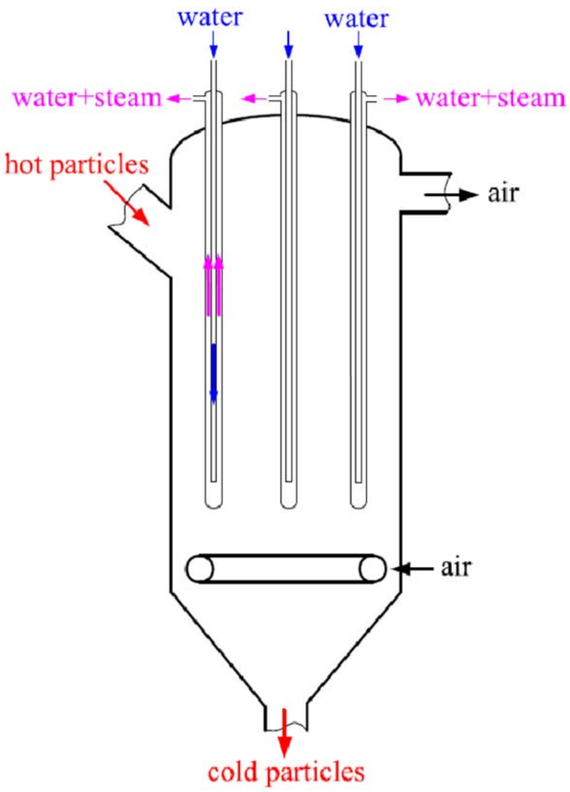

Figure 1. Schematic of a typical FCC dense-bed external catalyst cooler.

[Color figure can be viewed in the online issue, which is available at wileyonlinelibrary.com.]

particle convection component during contact with dense packet/emulsion phase and h_{rad} is the radiation component. Generally, the radiation component is insignificant when bed temperature is below 500°C.[13–15] Moreover, particle convection usually plays a more dominant role than gas convection as the heat capacity of solids is far higher than that of gas.[16] If h_{rad} and h_{g} are considered to be unimportant, Eq. 1 can be simplified into

$$h \approx \delta_{\mathrm{pa}} h_{\mathrm{p}} \tag{2}$$

To date, there have been numerous efforts paid to investigate bed-to-wall heat transfer in gas-solids fluidized beds as seen in the review of Chen.[13,16] However, most of these studies associated with dense fluidized beds (especially experimental studies) were conducted in fluidized beds with bigger Geldart B or D particles.[17,18] Only a few published studies on bed-to-wall heat transfer in fluidized beds of Geldart A particles can be found in literature, which are more useful in understanding the inner heat transfer mechanism and improving the design of FCC external catalyst coolers.

Lechner et al.[19] investigated the heat transfer between the fluidized Geldart A lignite particles and horizontal heat tube bundles. The effects of tube diameter, particle diameter, and the arrangement of tube bundles on heat-transfer coefficients were measured and correlated with heat-transfer coefficient. Di Natale et al.[20] experimentally studied the effect of different types of Geldart A particles and different surface types on bed-to-wall heat transfer. They found that the heat-transfer coefficient increased with increasing particle Archimedes number and was almost independent of particle thermal conductivity. The shape of the immersed object had a relevant influence on the heat-transfer coefficient, giving rise to a 30% difference in its value under high particle Archimedes numbers. Stefanova et al.[21,22] used an electrically heated vertical tube to measure the bed-to-wall heat-transfer coefficient in a fluidized bed with FCC particles. They found that the maximum heat-transfer coefficient occurred at a superficial gas velocity near the transition point of the turbulent flow regime. Moreover, they compared the effect of bed scale on bed-to-wall heat transfer in two columns of ID 0.29 and 1.56 m. The maximum heat-transfer coefficient was found to be unaffected by column diameter, but it occurred at higher superficial velocities in larger columns.

Recently, we built a cold-model FCC external catalyst cooler with vertical finned heat tubes.[23] By measuring the inlet and outlet water temperatures flowing through a heat tube, its wall temperature and the bed temperature, its bed-to-wall heat-transfer coefficients under different operating conditions could be determined. Moreover, a heat transfer intensification method was proposed by a double-distributor design to enhance the internal solids circulation. The measured higher heat-transfer coefficients partially validated its feasibility. However, the used heat tubes were fixed and could not move radially. The tube number was too few and the tube structure was too complex. The adopted measurement method could only determine the total heat-transfer coefficient of a heat tube, but the axial distribution of the bed-to-wall coefficient could not be obtained. These factors all limited a systematic understanding of the heat transfer properties of FCC external catalyst coolers.

To obtain deeper insights and comprehensive understanding of the heat transfer properties and their mechanisms insides FCC external catalyst coolers, a specially designed electrically heated copper tube was designed in this study. It has multiple sections as well as a lot of thermocouples for tube wall temperature measurement. Moreover, this tube can move freely along the radial direction. If inserted in a fluidized bed of FCC particles, both axial and radial profiles of heat-transfer coefficients can be determined. Moreover, in view of the close relationship between heat transfer properties and hydrodynamics in bed, an optical fiber probe was used to measure the surface gas-solids hydrodynamics on heat tube surface. Based on the widely accepted packet renewal model for bed-to-wall heat transfer,[24] a data processing method was proposed to determine the two important parameters on heat transfer properties, that is, the packet fraction and the mean packet residence time. With these two parameters, the bed-to-wall heater transfer mechanism in fluidized beds of fine Geldart A particles can be more deeply understood. Finally, we compared the experimental measured heat-transfer coefficients and those calculated from the packet renewal model[24] based on the measured packet fraction and mean packet residence time to analyze the feasibility of the data processing method of this study.

Experimental

Experimental unit

Experiments were implemented in a fluidized-bed column of ID 0.286 m, as schematically shown in Figure 2. The total column height was 6 m. Compressed air was supplied as the fluidizing gas by a Roots blower. The gas flow rate was regulated by a rotameter. After passing through a bottom

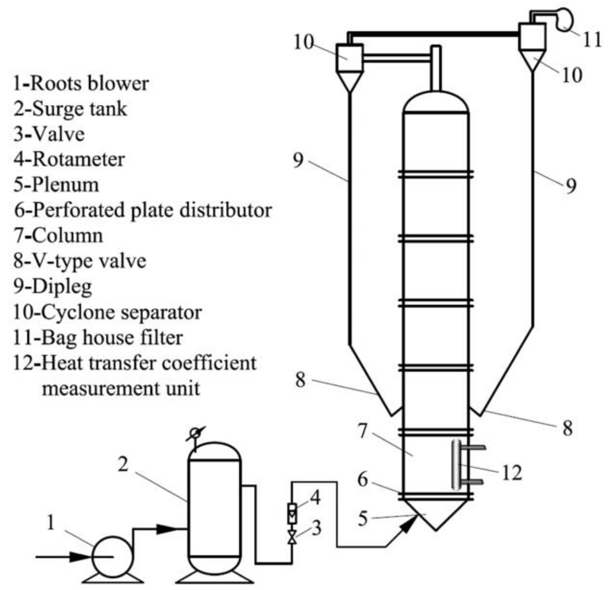

Figure 2. Schematic of the experimental unit.

plenum, air was distributed by a perforated plate distributor, which had an open area ratio of 0.9%. FCC equilibrium catalysts (not fresh catalysts) of mean diameter of 69.4 μm and particle density 1500 kg/m^3 were used as the fluidized particles, which were from a FCC unit in the Yanshan Refinery of Sinopec in Beijing. They corresponded to the solids properties in steady unit operation. Particles entrained by air were collected by two cyclone separators in series. The collected particles were returned into the bed via two diplegs. Each dipleg was equipped with a V-type valve to avoid gas bypassing through the cyclone dipleg and ensure steady particle flowing downward into the bed. The total particle collection efficiency of the two-stage cyclones was high enough to guarantee the solids inventory and the particle-size distribution unchangeable in a long operating period. The particles escaping from the exit of the second-stage cyclone were collected by a bag house filter to avoid particulate emission into the atmosphere. Two static bed heights of 0.6 and 1.1 m were used to study the effect of bed height. The superficial gas velocity in this study ranged from 0.1 to 0.5 m/s, a big range capable of covering the operating conditions of most dense external catalyst coolers in industrial FCC units. The heat-transfer coefficient measurement unit, as described in detail later, was installed in the bottom of the dense bed. The operating temperature, pressure, humidity, and so forth in the experiment were different from industrial catalyst coolers, which will influence the gas density, gas viscosity and thus the gas convective heat transfer. However, it is the particle convection that plays a dominant role in bed-to-wall heat transfer in fluidized heat exchangers of fine Geldart A particles. Therefore, it is expected that the trends of heat-transfer coefficients with gas velocity, axial, and radial positions will not change as a result of change in gas properties, although the measured total heat-transfer coefficients may be a little different.

Table 1. Summary of the Key Unit Structural Parameters, Operating Conditions, Gas and Solids Properties

Item	Value
1. Unit structural parameter	
Column inner diameter, m	0.286
Total column height, m	6.0
Static bed height, m	0.6, 1.1
Gas distributor type	Perforated plate distributor
Open area ratio	0.9%
Cyclone number	2
Cyclone connection type	In-series
2. Operating condition	
Superficial gas velocity, m/s	0.1$\sim$0.5
3. Gas and solids properties	
Gas type	Compressed air
Solids type	FCC equilibrium catalyst
Particle mean diameter, μm	69.4
Particle density, kg/m^3	1500
Particle bulk density, kg/m^3	929

A summary of the key unit structural parameters, operating conditions, gas and solids properties is listed in Table 1.

Measurement of heat-transfer coefficient

The bed-to-wall heat-transfer coefficients were measured by a specially designed measurement unit shown in Figure 3. Its key components were five electrically heated copper tubes of OD 0.04 m and length 0.12 m. A single copper tube was made of heating wire, toughened glass tube, copper shell, and thermocouples. Its detailed structure is illustrated in Figure 4. The heating wire connected to a DC power supply provided accurate data for the inputted heat flux. The heating wires were winded around the center glass tube. Heat-resistance adhesive was used to bond the glass tube and copper shell together and keep electric insulation simultaneously. Two T-type thermocouples were used to measure the wall temperature of the heat tube. Due to high thermal conductivity of copper, copper shell was selected to guarantee an even wall temperature. To simultaneously measure five heat-transfer coefficients at different heights, an insulation section made of Teflon plastics was installed between two neighboring heated copper tubes to minimize heat loss. The OD and length of an insulation section were 0.04 and

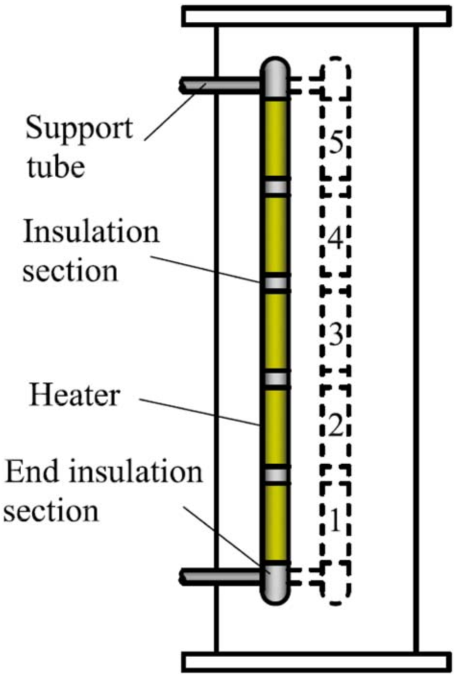

Figure 3. Schematic of the used heat-transfer coefficient measurement unit.

[Color figure can be viewed in the online issue, which is available at wileyonlinelibrary.com.]

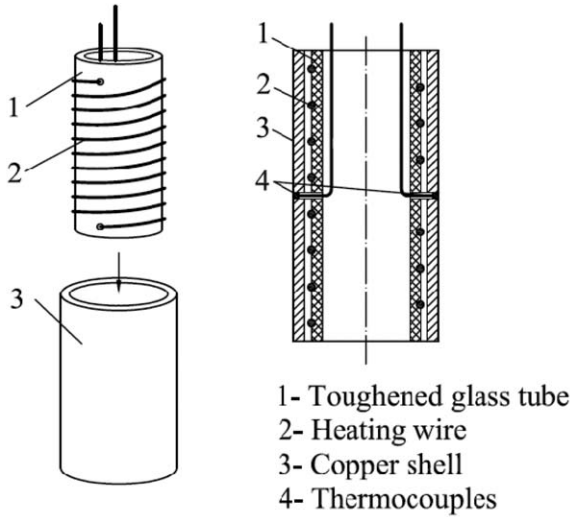

Figure 4. Schematic of the internal structure of a single heated copper tube.

0.025 m, respectively. There were also two semi-spherical Teflon caps for heat insulation. The heated copper tubes, insulation sections, and Teflon caps were connected together by several fastening screws. Two small horizontal stainless steel tubes connected with the two insulation tube caps supported the whole vertical heat tube and allowed its free movement radially. The horizontal tubes were connected to the column wall by a threaded flange and gasket, which were used to avoid gas or particles leakage. All the wires connecting heating wires and thermocouples led out of the column through the hollow support tubes and glass tubes in the heat tubes. From bottom to top, the five heated copper tubes were named as Heater #1–#5, as shown in Figure 3. Their axial positions (center) were 0.222, 0.367, 0.512, 0.657, and 0.802 m above the bottom gas distributor, respectively. There were six radial measurement positions at $r/R_w = 0, 0.3, 0.6, 0.8, 0.9, 0.95$. Here, r is the radial position of the center of the heater tube and R_w is the maximum radial position that the heater tube can reach, that is, the column radius minus the radius of the heat tube (0.123 m).

For each heated copper tube, there were two corresponding rod-shape thermocouples used to measure the bed temperatures. Their lateral installation locations relative to the heat-transfer coefficient measure unit are shown in Figure 5. One thermocouple was located at 90° position and the other was at 180° position relative to the heat-transfer coefficient measurement unit. Their insertion lengths into the bed were 60 and 30 mm from the wall, respectively. They were installed at the same axial positions to the centers of the five heat tubes. When the bed reached a steady fluidization state, data for the voltage of the heating wires and the copper tube wall temperatures were logged for 5–10 min at an interval of 1 s by a Visual Basic data-acquisition program. The bed temperatures were also simultaneously logged from the rod-shape thermocouples. Their sample period and frequency were the same as the thermocouples attached on the heat tube surface.

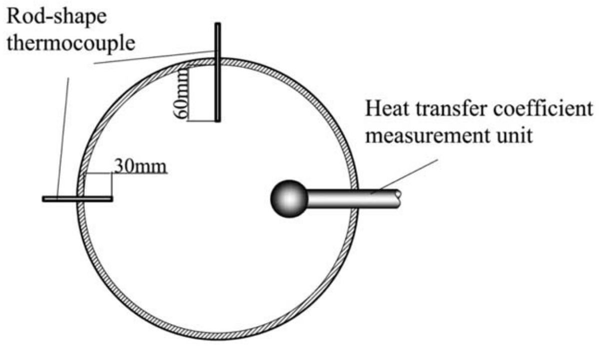

Figure 5. Lateral installation locations of the two rod-shape thermocouples for bed temperature measurement.

The bed-to-wall heat-transfer coefficient was calculated by

$$h = \frac{Q_{\mathrm{in}}}{A(T_w - T_b)} = \frac{U_h^2/R}{A(T_w - T_b)} \tag{3}$$

Here, Q_{in} is the input heat flux of the heating wire, U_h and R are the input voltage and resistance of the heating wire, respectively, A is the contacting area between the copper tube surface and the bed material, that is, the cylindrical area of the copper tube, T_w and T_b are the tube surface temperature and bed temperature, respectively. T_w is calculated from the average of the two temperatures obtained by the chip thermocouples glued on the tube surface. T_b is calculated from the average temperature from the two rod-shape thermocouples.

The heat-transfer coefficient calculated from Eq. 3 does not account for the axial heat loss emitted from the two end surfaces, resulting in an error and inevitably influencing the data accuracy. In the following, an error analysis based on a series of experimental results is conducted to evaluate the quantity of the error in this study. Take Heater #3 for example, a heat balance can be made as shown in Figure 6 and Eq. 4

$$Q_{\mathrm{in}} = Q_{\mathrm{out}} + Q_{R1} + Q_{R2} \tag{4}$$

Here, Q_{in} was the input heat flux by the heating wire in Heater #3, Q_{out} was the heat emitted from the cylindrical

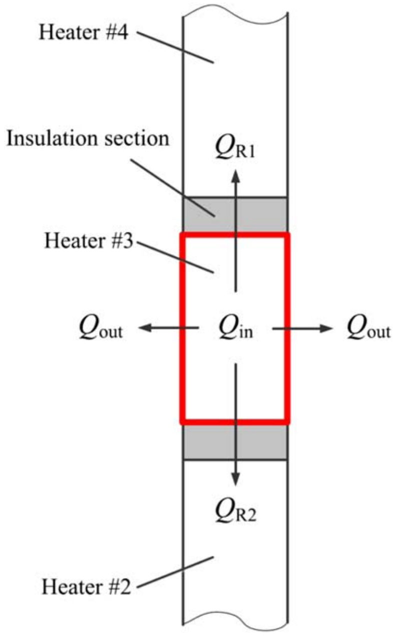

Figure 6. Heat balance of Heater #3.

[Color figure can be viewed in the online issue, which is available at wileyonlinelibrary.com.]

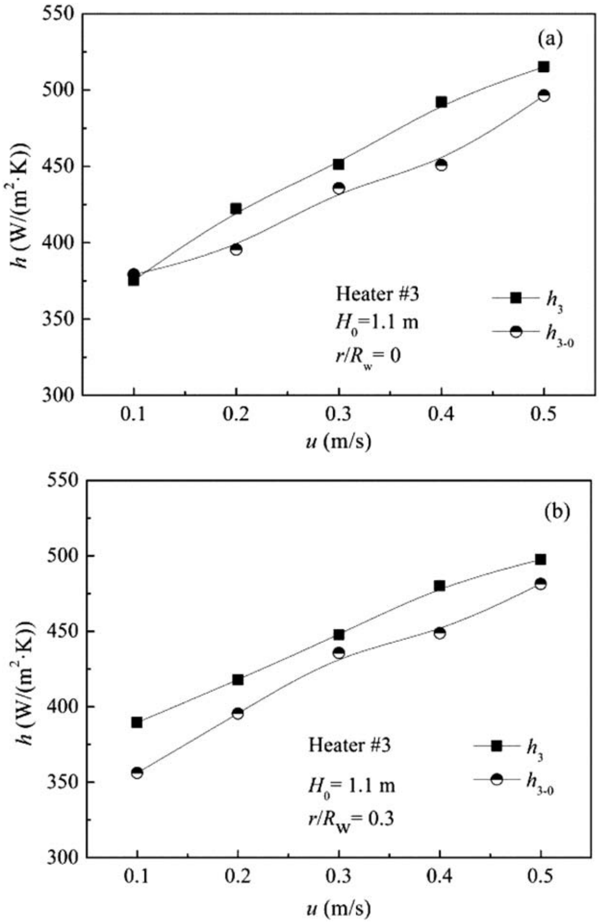

Figure 7. Comparison of the measured heat-transfer coefficients with maximum and minimum errors.

surface into the bed, Q_{R1} and Q_{R2} were the heat transferred from Heater #3 to Heaters #2 and #4 due to thermal conduction, respectively. Equation 4 can be further extended into

$$\begin{aligned} U_{h3}^2/R_3 = {} & h_{3-0}A_3(T_{w3}-T_b)+h_{2-3}A_{2-3}(T_{w3}-T_{w2}) \\ & +h_{4-3}A_{4-3}(T_{w3}-T_{w4}) \end{aligned} \tag{5}$$

Here, $h_{3\text{-}0}$ represents a more accurate value than that computed from Eq. 3, $h_{2\text{-}3}$, $h_{4\text{-}3}$, $A_{2\text{-}3}$, $A_{4\text{-}3}$ are the heat-transfer coefficients and areas from Heater #3 to Heaters #2 and #4. As heat conduction is more important and the relative heat transfer area is small, the heat loss from the cylindrical surface of the insulation sections is omitted in Eq. 5. It can be concluded from Eq. 5 that the error is minimized if T_{w2} and T_{w4} are kept same as T_{w3} and the error is maximized if the heating wires in Heaters #2 and #4 are switched off and T_{w2} and T_{w4} are approaching to the bed temperature T_b.

Based on the above analysis, two sets of calibration experiment were conducted. In one set of calibration, Heaters #2∼#4 were all switched on. After the wall temperature of Heater 3 was stabilized, the powers of Heaters #2 and #4 were finely adjusted to maintain their wall temperatures T_{w2} and T_{w4} to equal T_{w3}. In the other set of calibration, only Heater #3 was switched on. Figure 7 compared the typical heat-transfer coefficients measured at two radial positions during the two sets of calibrations. Here, $h_{3\text{-}0}$ and h_3 represent the measured heat-transfer coefficients at $T_{w2}{\approx}T_{w3}{\approx}T_{w4}$ and $T_{w2}{\approx}T_b{\approx}T_{w4}$, respectively. As shown in Figure 7, h_3 is generally higher than $h_{3\text{-}0}$ as the heat loss is included in Q_{in}. However, their relative errors fluctuate in a small range and the maximum error is only 9.7%, which corresponds to a maximum temperature difference of 15°C between T_{w3} and T_{w2} or T_{w4}. This demonstrates that the insulation sections used in the heat-transfer coefficient measurement unit were effective to minimize heat loss through the two end surfaces.

In our later experiments, the five heaters were all switched on to increase measurement efficiency. Table 2 shows two typical sets of data for the measured bed temperatures, tube wall temperatures and input powers of the five heaters. It can be seen that the bed temperatures are nearly uniform, only in a small fluctuation range of 1–2°C. This further demonstrates that a fluidized bed is approaching to an isothermal reactor due to the violent solids mixing. As a result of different power inputs, the wall temperatures of the five heaters can be controlled to be nearly equal. The fluctuation range of T_w in Table 2 is less than 2.5°C and less than 5°C throughout the experimental results. As seen in Eq. 5, Q_{R1} and Q_{R2} are proportional to the temperature difference. Therefore, it can be concluded the relative errors of the measured heat-transfer coefficients should be no more than 30% of the maximum error in Figure 7, corresponding to a relative error less than 3%, which validates the reliability of this measurement method.

Measurement of tube surface hydrodynamics

In previous published literatures on fluidized-bed heat transfer, most researchers[16,25–29] chose to correlate the dimensionless number Nu_p by Re_p, Ar, superficial gas velocity, voidage, bed temperature, and so forth to obtain quantitative predictions of heat-transfer coefficients. Few studies[17,30,31] were on the surface hydrodynamics, which is directly related to bed-to-wall heat transfer mechanism. Based on the famous packet renewal theory proposed by Mickley and Fairbanks,[24] two surface hydrodynamic parameters, that is, time fraction of packet δ_{pa} and mean packet residence time τ_{pa} were most important in influencing heat-transfer coefficient. Their relation with heat-transfer coefficient can be expressed by

$$h=2\delta_{pa}\left[\frac{k_{pa}\rho_{pa}c_{pa}}{\pi\tau_{pa}}\right]^{1/2} \tag{6}$$

Table 2. Typical Measured Bed Temperatures, Tube Wall Temperatures, and Input Powers

	Case 1			Case 2		
Heater	T_w (°C)	T_b(°C)	Q_{in}(W)	T_w(°C)	T_b(°C)	Q_{in}(W)
#1	40.10	28.51	89.29	46.15	27.13	89.29
#2	40.08	28.53	84.33	45.32	26.92	84.33
#3	42.37	29.30	94.76	46.87	28.13	94.76
#4	40.21	29.06	84.88	43.15	27.04	84.38
#5	40.08	29.01	85.36	44.16	27.14	84.86

Note: Case 1: r/R_w=0.3, u=0.4 m/s, H_0=1.1 m; Case 2: r/R_w=0.9, u=0.3 m/s, H_0=1.1 m.

Here, k_{pa} is the thermal conductivity of packet, ρ_{pa} is the packet density, and c_{pa} is the heat capacity of packet. δ_{pa} is defined as the total residence time of packet divided by the total measurement time. τ_{pa} represents the average residence time of packet staying on heat tube surface. The reciprocal of τ_{pa} represents the renewal frequency of packet on heat tube surface. According to Eq. 6, high δ_{pa} and small τ_{pa} are favorable to high-efficiency bed-to-wall heat transfer. According to Mickley and Fairbanks,[24] δ_{pa} is written as

$$\delta_{pa} = \frac{\sum_{i=1}^{n} \tau_{pa,i}}{t} \tag{7}$$

and τ_{pa} is the root-square-average residence time

$$\tau_{pa} = \left[\frac{\sum_{i=1}^{n} \tau_{pa,i}}{\sum_{i=1}^{n} \sqrt{\tau_{pa,i}}} \right]^2 \tag{8}$$

Based on the measured particle concentration signals by a capacitance probe, Chandran and Chen[31] determined δ_{pa} and τ_{pa} on the surface of a horizontal heat tube using a critical voidage of 0.8. Kim et al.[30,32] used a transmission-type optical fiber probe to detect the bubble and emulsion fractions and frequencies whose critical light intensity used to distinguish between bubble and emulsion phase was the average of the maximum and minimum of the measured signals. In this study, a reflection type optical fiber probe developed by the Institute of Processing Engineering, Chinese Academy of Science[33] was used to detect the packet renewal behavior on the heat tube surface. As seen in Figure 8a, the optical fiber probe of OD 4 mm was horizontally inserted into a vertical stainless steel tube, which was used as a cold model of the heat tube shown in Figure 3 and had identical geometrical dimensions. The face of the probe tip was aligned to the cylindrical tube surface. The arrangement of the optical fibers in the probe tip is shown in Figure 8b. There were two squares (1×1 mm^2) where very fine optical fibers of diameter 20 μm were bundled. Fibers for emitting and receiving light were aligned alternatively in each square. The two squares could enable the velocity of particles or bubbles measured with this probe. Before sampling, the probe was first calibrated by an opaque fixed-bed column with FCC particles. The particle concentration at bulk packing was tuned into a signal voltage of 4.3 V and the zero particle concentration was tuned into a signal voltage of 0 V. The signals were sampled with a sampling frequency of 3.906 kHz for each measurement of 8.35 s. To obtain better data repeatability, 20 times of repetitive measurements, that is, a total sampling time of 167 s, were conducted at each measurement point. During sampling, the fluidized-bed column was wrapped by a layer of blackout cloth to avoid the inference of the outside sun light. There were also five axial heights and six radial positions, that is, 30 points, selected for optical fiber probing. The five axial heights corresponded to the centers of the five heaters shown in Figure 3. The six radial positions were the same as in heat-transfer coefficient measurement.

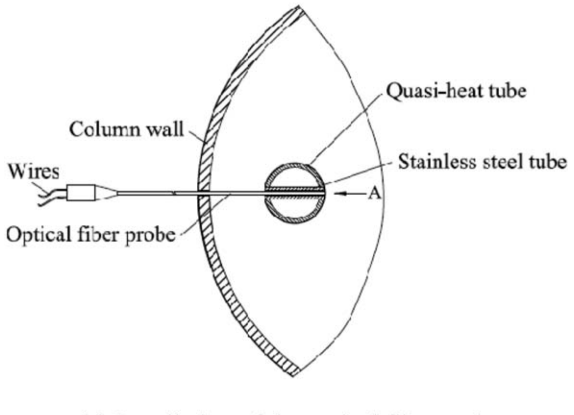

(a) Installation of the optical fiber probe

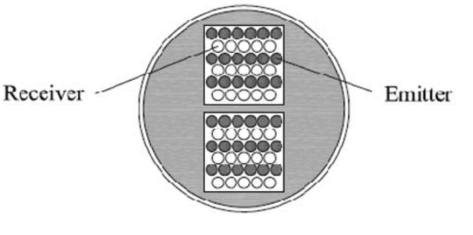

(b) Optical fiber arrangement at the tip of the probe

Figure 8. Used optical fiber probe and its installation for tube surface hydrodynamics measurement: (a) installation of the optical fiber probe; (b) optical fiber arrangement at the tip of the probe.

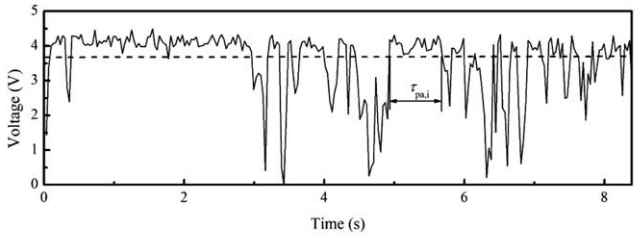

Figure 9. Typical measured instantaneous particle concentration signals.

Figure 9 shows typical measured instantaneous particle concentration signals. It is seen that there exists two phases, that is, bubble and packet (or called emulsion) as indicated by the signals below and above the dashed line in Figure 9. The packet phase has a relative constant voltage with small fluctuations. A packet of residence time $\tau_{pa,i}$ is illustrated in Figure 9. The bubble phase is comprised with many steep troughs, whose number or frequency can be clearly identified. However, it is possible that the signals of some very small bubbles may be overlapped in the packet signals and cannot be identified. Compared the measurement results of Chandran and Chen[31] by a capacitance probe, the two-phase nature of fluidized beds is more readily discernable here. The optical fiber probe is more sensitive, more difficult to be disturbed than a capacitance probe and thus more reliable in measured results.

The selection of a critical voltage or voidage value, that is, the position of the dashed line in Figure 9, is very important to obtain accurate surface hydrodynamic parameters and better modeled results of heat-transfer coefficients. In this study, we had tested many critical voltages to show their effect on the identified number of bubbles. Figure 10 is the results for the typical particle concentration signals measured at four different positions and in 167 s. It is seen that bubble numbers keep constant at $2.8 \text{ V} < U < 3.6$ V. A smaller voltage value less than 2.8 V will lose to accounting for some small bubbles. When the critical voltage value exceeds 3.6 V, the strong fluctuation of the packet phase will lead to a sudden increase in bubble numbers. In view of the two-phase nature of fluidized beds and the agreement with the observed trough numbers in the measured signals, a unified

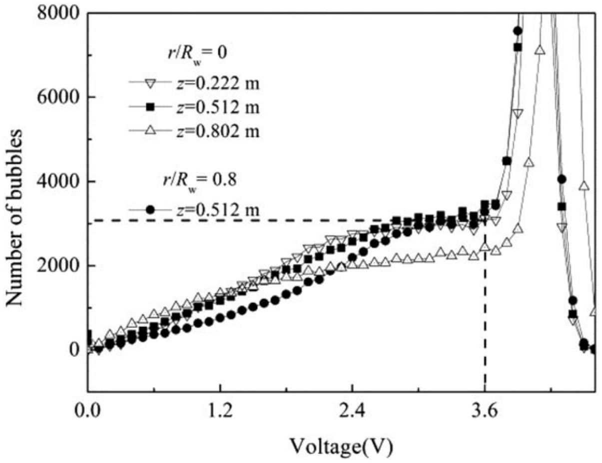

Figure 10. Determination of the critical voltage for distinguishing two phases.

critical voltage value of 3.6 V, corresponding to a voidage of 0.57, was used to calculate the τ_{pa} and δ_{pa} throughout the data processing. Comparatively, the critical voidages adopted by Chandran and Chen[31] and Kim et al.[30,32] were too small. They also seemed to be more or less subjective, casual, and thus less agreeable with experimental facts. To increase the efficiency of data processing, a MATLAB program was composed for batch data processing.

In this study, different gas-solids flow behaviors were easily observable on heat tube surface and in bed if the optical fiber probe tips protruded slightly outside the tube surface. Figure 11 shows the particle concentrations measured on heat tube surface and in bed. It is seen that the measured particle concentrations were almost the same when the probe tip was aligned to and 3 mm away from the cylindrical tube surface. However, a sudden decrease in particle concentration was clearly seen when the probe tip protruded 8 mm away as seen in Figure 11. At higher superficial gas velocities, this phenomenon was more readily observable. It is demonstrated that improper positioning of measurement points can lead to wrong tube surface hydrodynamic results which may be irrelevant to heat transfer properties. Stefanova et al.[22] used the measured local voidage signals above and below their heater tube to analyze the effect of gas-solids flow behavior on the heat-transfer coefficient at different superficial gas velocities. Based on our analysis, it is very doubtful that their measured hydrodynamics were correlated to their heat transfer properties. It is also inferred from Figure 11 that there is a static layer of solids with a thickness between 3 and 8 mm on the tube surface. To better represent the solids packet renewal behavior, it is strongly suggested that the probe tip is in this static solids boundary layer.

When using the optical fiber probe to determine the actual particle concentration, it is often suggested that a calibration is conducted as the measured voltage signal is believed not to be linear to the actual solids volume fraction.[34] In this study, we also conducted a simple calibration by correlating the measured particle concentrations by differential pressure transducers to the area-averaged particle concentrations based on integrating the measured point results by the optical fiber probe. Equation 9 is the calibrated exponential correlation for voidage ε and voltage U

$$\varepsilon = 1 - 0.06\exp(0.55U) \tag{9}$$

Results and Discussion

Relative positions of the heaters at different static bed heights

In this study, the expanded bed heights at different superficial gas velocities were determined by the measured total bed pressure drop and another pressure drop across a distance of Δh in the dense bed. The correlation of the expanded bed height H_f is

$$H_f = \frac{p_A - p_C}{p_A - p_B}\Delta h \tag{10}$$

Here, p_A, p_B, p_C are the gauge pressures measured at the bottom of the dense bed, in the middle of the dense bed, and in freeboard, respectively. Δh is the height between the two pressure taps of p_A and p_B. It is noted that a constant particle concentration is assumed in this calculation. Moreover, part of pressure drop between the bed surface and the pressure tap of p_C is included in Eq. 10, resulting in a slight overestimation in the calculated H_f. However, as the operating gas velocities in this study are relatively small, the effect of this part of pressure drop is negligible. Figure 12 shows the

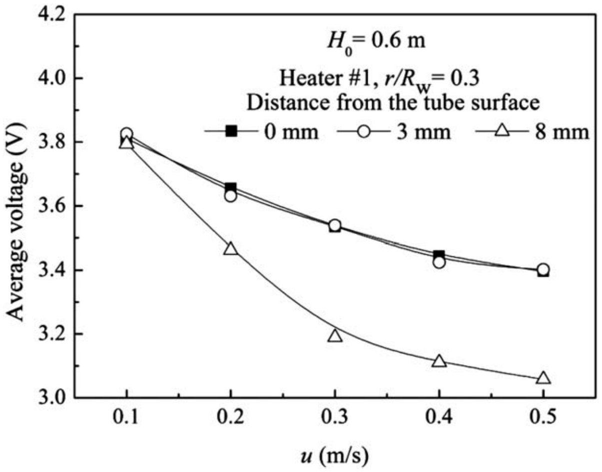

Figure 11. Different particle concentrations measured on heater tube surface and in bed.

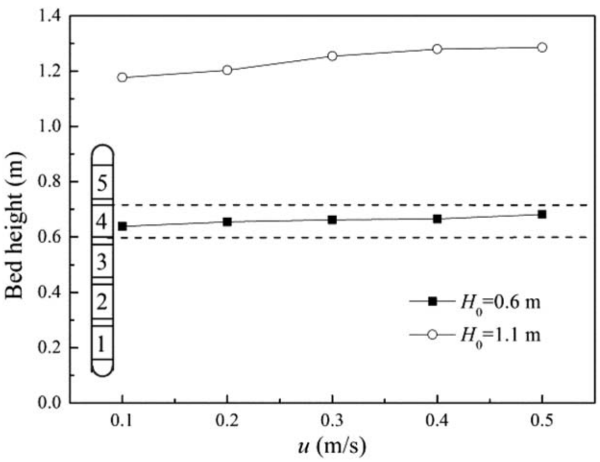

Figure 12. Bed expansions at different static bed heights.

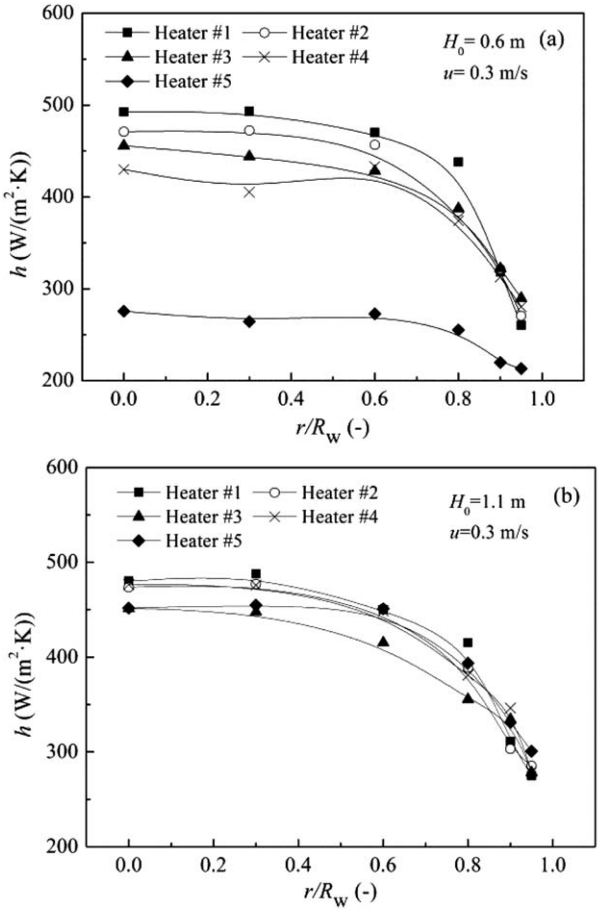

Figure 13. Typical radial profiles of heat-transfer coefficient at different heights.

expanded bed heights at different superficial gas velocities. The relative positions of the five heaters are also drawn in Figure 12. It is seen that H_fs at both $H_0 = 0.6$ m and 1.1 m increase slowly with increasing superficial gas velocity. The net bed expanded heights are all small. At $H_0 = 0.6$ m, Heater #4 became gradually submerged in the dense bed as the superficial gas velocity increases. Heater #5 was always in freeboard even at the highest superficial gas velocity. At $H_0 = 1.1$ m, all five heaters were immersed in the dense bed at all superficial gas velocities.

Radial profiles of heat-transfer coefficients and packet parameters

Figure 13 shows typical radial profiles of the measured heat-transfer coefficients at $u = 0.3$ m/s. In center of the dense bed ($r/R_w \leq 0.6$), the measured heat-transfer coefficients are higher and independent of the radial position. As the heat tube approaches to the column wall ($r/R_w > 0.6$), the measured heat-transfer coefficient decreases with increasing speed. This is consistent with previous experimental results in fluidized beds of both Geldart A and B particles.[22,35] This radial difference in heat-transfer coefficient could be explained by our measured tube surface hydrodynamics based on the packet renewal theory.[24] Figure 14 shows typical particle concentration signals measured at different radial positions. It can be seen that there are more bubbles in the bed center than near the wall, which corresponds to more frequent packet renewal on tube surface in the bed center. Due to wall effect, bubbles choose to dodge the near-wall region, which enables packets to stay on tube surface longer and become a resistance of heat transfer.

The heat-transfer coefficients shown in Figure 13 are insensitive to the axial positions in the dense bed, especially at higher static bed. This indicates that solids in the dense bed mix violently, enabling it to be viewed as an isothermal reactor. At $H_0 = 0.6$ m, the dense bed can only partially submerge Heater #4 and can never submerge Heater #5. Therefore, the heat-transfer coefficients measured by Heater #5 in Figure 13a are greatly lower than by other heaters.

The radial profiles of packet fraction and mean packet residence time determined from the particle concentration signals are further provided in Figures 15 and 16, respectively, to reveal the relationship between heat transfer properties and tube surface hydrodynamics. Both the packet fraction and mean packet residence time are lower in the bed center and higher in the near wall region. According to the packet renewal theory,[24] a higher packet fraction indicates a longer contact time between packet and heat transfer surface, which is favorable to higher heat-transfer coefficient. A higher mean packet residence time represents less frequent packet renewal on heat transfer surface, which is disadvantageous to higher heat-transfer coefficient. It is found that the radial profiles of packet fraction shown in Figure 15 are conflicting to the results of Figure 13. However, the radial profiles of mean packet residence time shown in Figure 16 are consistent to Figure 13. The sudden increase of τ_p at $r/R_w > 0.6$ is also agreeable to the sudden decrease in heat-transfer coefficient shown in Figure 13. This indicated that the packet renewal frequency played a more dominant role in bed-to-wall heat transfer than packet fraction and enhancing stronger solids circulation should be a more effective method for bed-to-wall heat transfer intensification.

For Heater #5 at $H_0 = 0.6$ m, both the packet fraction and mean packet residence time are much smaller than other heaters. According to the above analysis, its heat-transfer coefficients should be the highest. Figure 17 shows a typical instantaneous particle concentration signal measured on the tube surface of Heater #5. It can be seen that it has a different flow behavior from those as shown in Figure 14. The difference originates from the different measurement locations. At $u = 0.3$ m/s, Heater #5 was in freeboard and Heater #3 was in the dense bed. The small fraction of high voltage

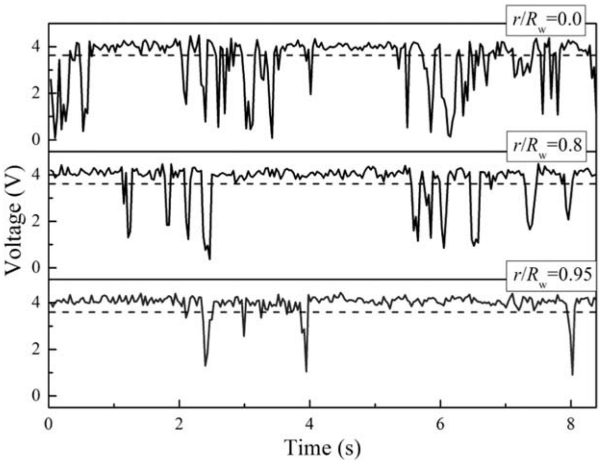

Figure 14. Typical instantaneous local particle concentration signals measured at different radial positions ($u = 0.3$ m/s, Heater #3).

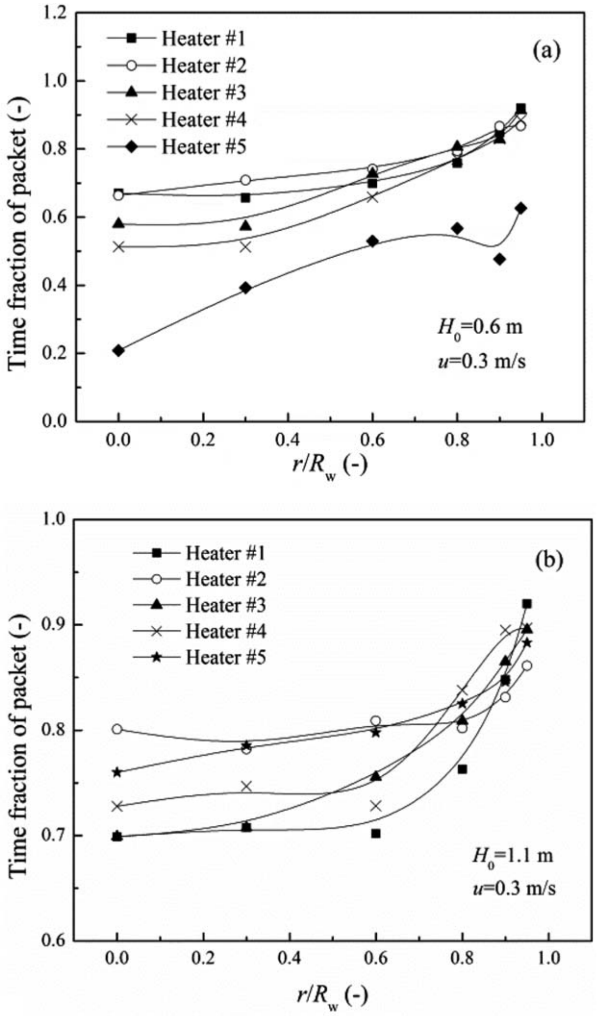

Figure 15. Radial profiles of packet fraction at different heights.

signals in Figure 17 is a result of particle splashing due to bubble breakage. Although the mean packet residence time is small, the total packet contacting time with the tube surface is not long. Here, the packet fraction plays a more dominant role on bed-to-wall heat transfer. By comparing the different heat transfer behavior in the dense bed and freeboard, it is speculated that the effect of packet fraction on heat-transfer coefficient should not be linear as in Eq. 6. It is more likely that it is a function of both packet fraction and residence time. Therefore, Eq. 6 should be modified into

$$h=2f\left(\delta_{\mathrm{pa}},\ \tau_{\mathrm{pa}}\right)\left[\frac{k_{\mathrm{pa}}\rho_{\mathrm{pa}}c_{\mathrm{pa}}}{\pi\tau_{\mathrm{pa}}}\right]^{1/2} \tag{11}$$

When the packet residence time is short, $f(\delta_{\mathrm{pa}},\ \tau_{\mathrm{pa}})$ may be a linear function. However, it may be a nonlinear function of packet fraction when the packet residence time is long, because the long residence of packet on heat transfer surface may become heat transfer resistance and negatively affect the heat-transfer coefficient. An example of this situation is in the dense bed of a bubbling fluidized bed operated at a low superficial gas velocity. The above content is just a first speculation, the determination of the exact expression of $f(\delta_{\mathrm{pa}},\ \tau_{\mathrm{pa}})$ still needs more modeling work and experimental validations.

Effect of superficial gas velocity

The effect of superficial gas velocity on the radial profiles of heat-transfer coefficients is shown in Figure 18. Similar radial distributions are found in Figure 13. Increasing the superficial gas velocity results in higher heat-transfer coefficients. At different radial positions, the effects of superficial gas velocity are different. Compared to the near wall region, it is more effective to increase heat-transfer coefficient by increasing superficial gas velocity in the bed center. Figure 19 shows typical instantaneous particle concentration signals on the tube surface at different superficial gas velocities. The increase of bubble number can be clearly observed at higher superficial gas velocities, which indicate more frequent packet renewal on heat transfer surface and thus is consistent to the increased heat-transfer coefficients.

Considering the different heat-transfer coefficients at different radial and axial positions, the averaged heat-transfer coefficient as a function of superficial gas velocity is drawn in Figure 20. For both $H_0 = 0.6$ m and 1.1 m, the averaged heat-transfer coefficient increases with increasing superficial gas velocity. There is no maximum in the two curves, slightly different from previous reports.[21,22] For fine Geldart A particles, the location of the maximum heat-transfer coefficient was reported to be near the onset of the turbulent flow

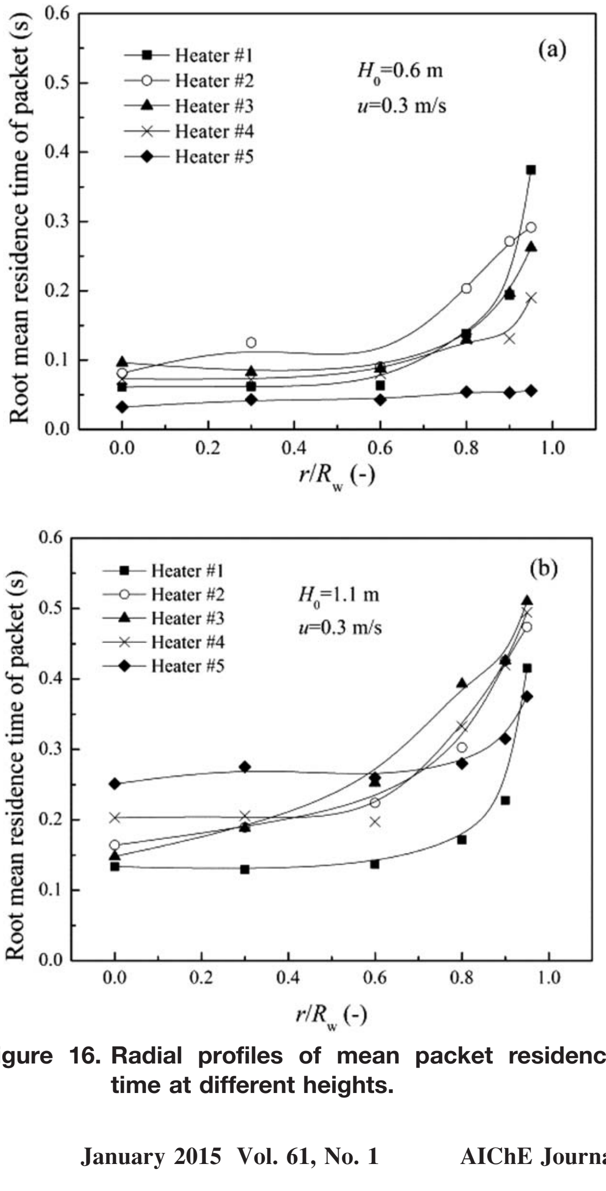

Figure 16. Radial profiles of mean packet residence time at different heights.

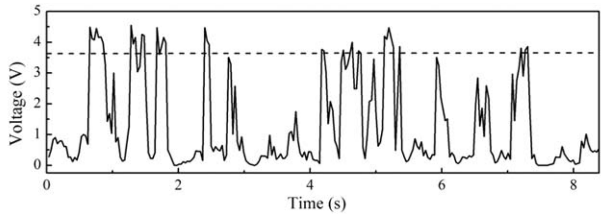

Figure 17. Typical instantaneous local particle concentration signals measured on the tube surface of Heater #5 ($H_0 = 0.6$ m, $u = 0.3$ m/s).

regime.[21,22] It seems that the range of superficial gas velocity in this study was not wide enough to span the turbulent flow regime.

The radial profiles of packet fraction and mean packet residence time keep similar trends at different superficial gas velocities as shown in Figures 21 and 22. They are still smaller in the bed center and gradually increase as the heat tube approaches to the column wall. As superficial gas velocity increases, both packet fraction and mean packet residence time decrease. At a higher static bed height, this trend is more pronouncedly seen in Figures 21b and 22b. Based on the packet renewal theory,[24] only the change of mean packet residence time with superficial gas velocity is consistent to the change of heat-transfer coefficient in Figures 18 and 20. Again, the predominant role of packet renewal frequency is demonstrated.

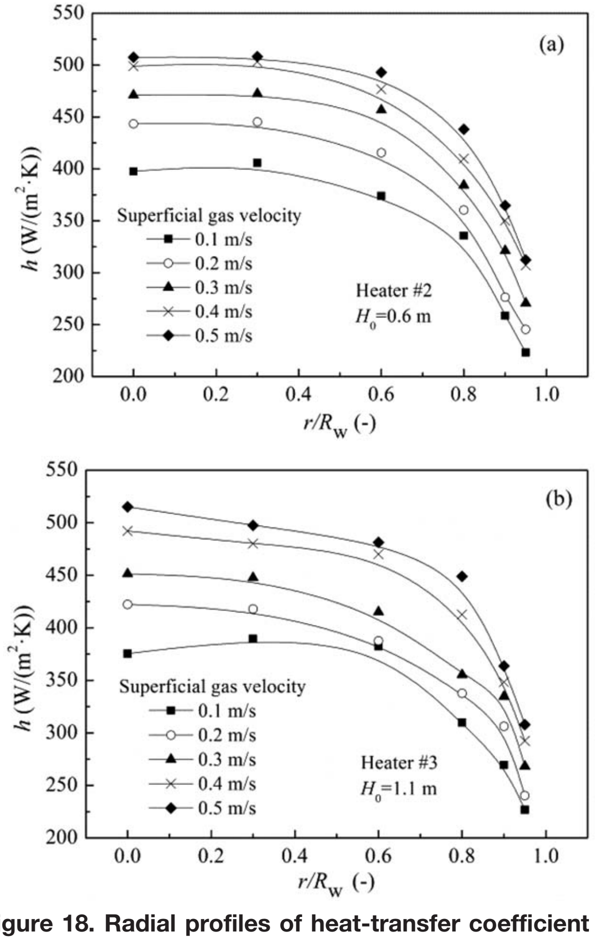

Figure 18. Radial profiles of heat-transfer coefficient at different superficial gas velocities.

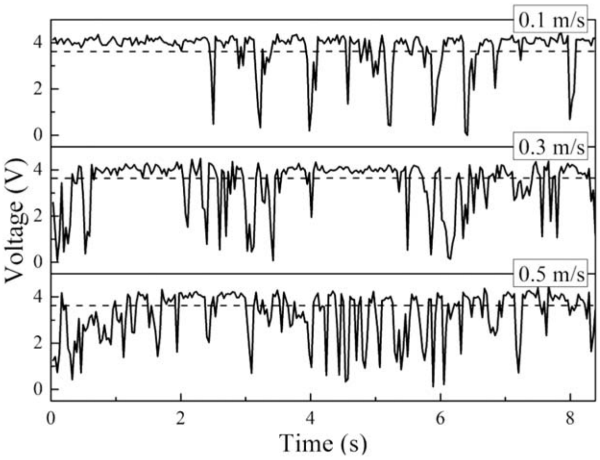

Figure 19. Typical instantaneous local voltage signals measured at different superficial gas velocities ($r/R_w = 0$, Heater #3).

Effect of static bed height

Figure 23 shows the effect of static bed height on the local heat-transfer coefficients. It is clear that the difference between the heat-transfer coefficients measured at Heaters #2 and #3, that is, at higher axial positions, is small at $H_0 = 0.6$ m and 1.1 m. However, there are large differences between the heat-transfer coefficients measured at Heater #1, that is, in the bottom of the dense bed. As seen in Figures 23g, h, the two radial positions in the bed center have the largest differences between the two measured heat-transfer coefficients. The differences at the two radial positions decrease with increasing gas velocity, consistent to the change of average heat-transfer coefficient shown in Figure 20. However, the heat-transfer coefficient difference near the wall, that is, at $r/R_w = 0.95$ (see Figure 23i) is not remarkable.

The effect of static bed height on heat-transfer coefficient can also be observed and explained by the measured tube surface hydrodynamics. Figure 24 compares the measured packet parameters of Heater #1 at $H_0 = 0.6$ m and 1.1 m. The selection of Heater #1 in Figure 24 is due to the big differences in their measured heat-transfer coefficients in the bed bottom. As superficial gas velocity increases, the packet

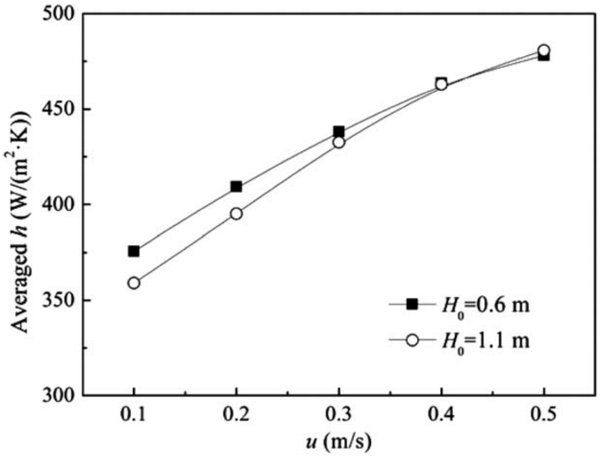

Figure 20. Average heat-transfer coefficients as a function of superficial gas velocity.

fraction and mean packet residence time follow a similar increasing trend as those shown in Figures 15, 16, 21, and 22. Comparatively, the differences in packet fraction at $H_0 = 0.6$ m and 1.1 m are relatively small. However, the mean packet residence times at $H_0 = 0.6$ m are smaller than those at $H_0 = 1.1$ m at $r/R_w = 0$ and 0.8. This corresponds to the higher packet renewal frequency at the tube surface of Heater #1 and its higher heat-transfer coefficients, agreeable with the change of heat-transfer coefficients shown in Figures 23g, h. The difference in mean packet residence time decreases with increasing superficial gas velocity, which is also agreeable with Figures 23g, h. At $r/R_w = 0.95$, the differences in mean packet residence time at different static bed heights are pretty small, which can also correspond to the small differences in heat-transfer coefficient shown in Figure 23i.

Discussion of the experimental results

With the determined packet fraction and mean packet residence time, the quantitative value of the heat-transfer coefficient can be calculated using Eq. 6 based on the packet renewal model.[24] This can also be used to testify the feasibility of the method used in this study for tube surface hydrodynamics measurement. Before the calculation, other parameters, that is, k_{pa}, ρ_{pa}, c_{pa}, must be primarily determined. ρ_{pa} equals to

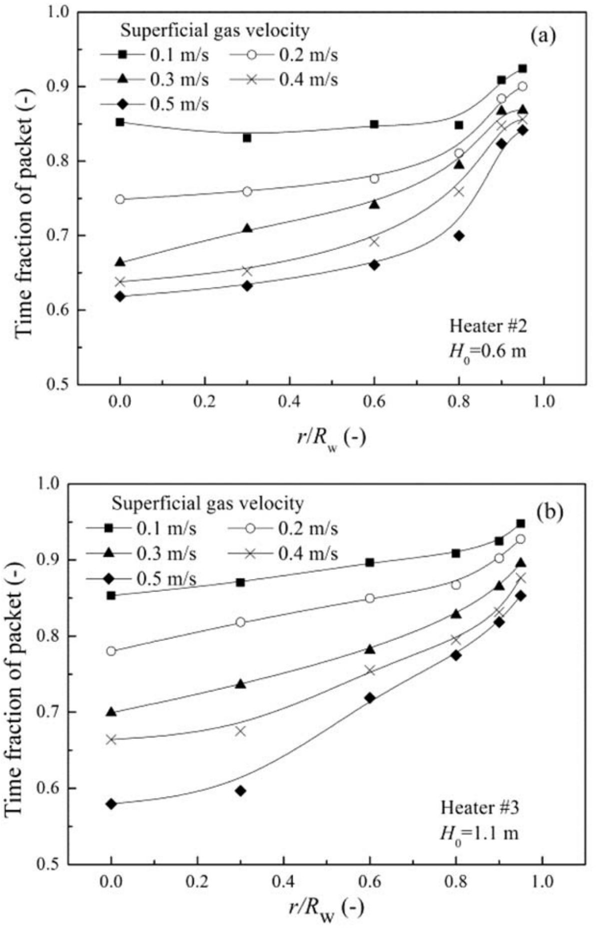

Figure 21. Radial profiles of packet fraction at different superficial gas velocities.

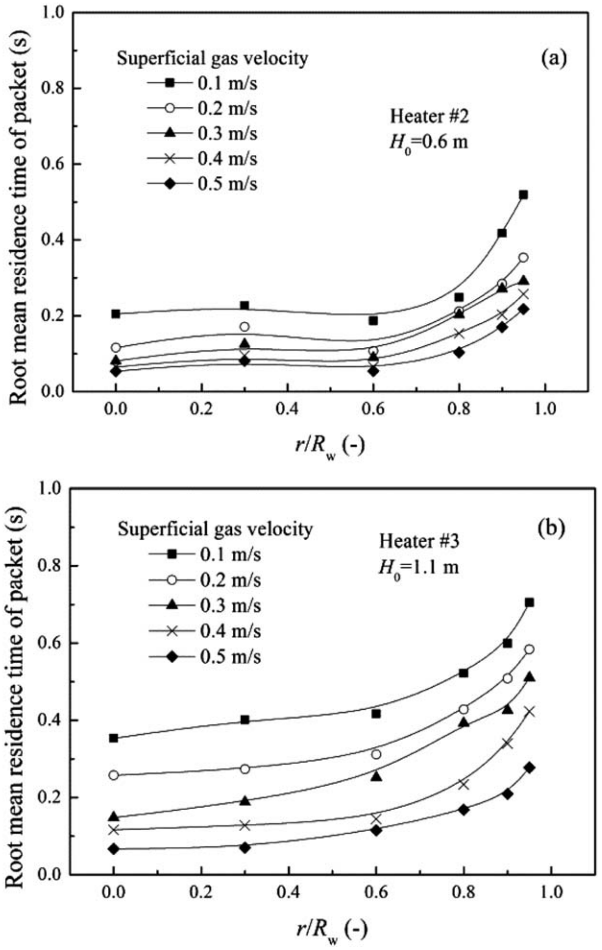

Figure 22. Radial profiles of mean packet residence time at different superficial gas velocities.

$$\rho_{pa} = \rho_p (1 - \varepsilon_{pa}) \tag{12}$$

Chen et al.[36] thought that ε_{pa} can be replaced by ε_{mf}, that is, the voidage at minimum fluidization. In this study, we followed a different approach. After data processing to distinguish packet and bubble phases, the average voltage of the packet phase was used to calculate the packet voidage using Eq. 9. In this study, we use the general model of Kunii and Smith[37] to calculate k_{pa}, that is

$$k_{pa} = k_g \left[\varepsilon_{pa} + \frac{(1-\varepsilon_{pa})}{\phi_k + 2k_g/3k_s} \right] \tag{13}$$

where ϕ_k is given by

$$\phi_k = 0.305 \left(\frac{k_s}{k_g} \right)^{-0.25} \quad \text{for } 1 \le \frac{k_s}{k_g} \le 1000 \tag{14}$$

This was also the same method used by Chandran and Chen.[37] The heat capacity of packet, c_{pa} is estimated by

$$c_{pa} = \frac{\varepsilon_{pa} c_{pg} \rho_g + (1-\varepsilon_{pa}) c_{ps} \rho_p}{\varepsilon_{pa} \rho_g + (1-\varepsilon_{pa}) \rho_p} \tag{15}$$

As $\rho_g \ll \rho_s$, c_{pa} can be replaced by c_{ps}. To account for the variation in packet voidage within the transient conduction zone near the wall, Chandran and Chen[37] adopted a correction factor C written as

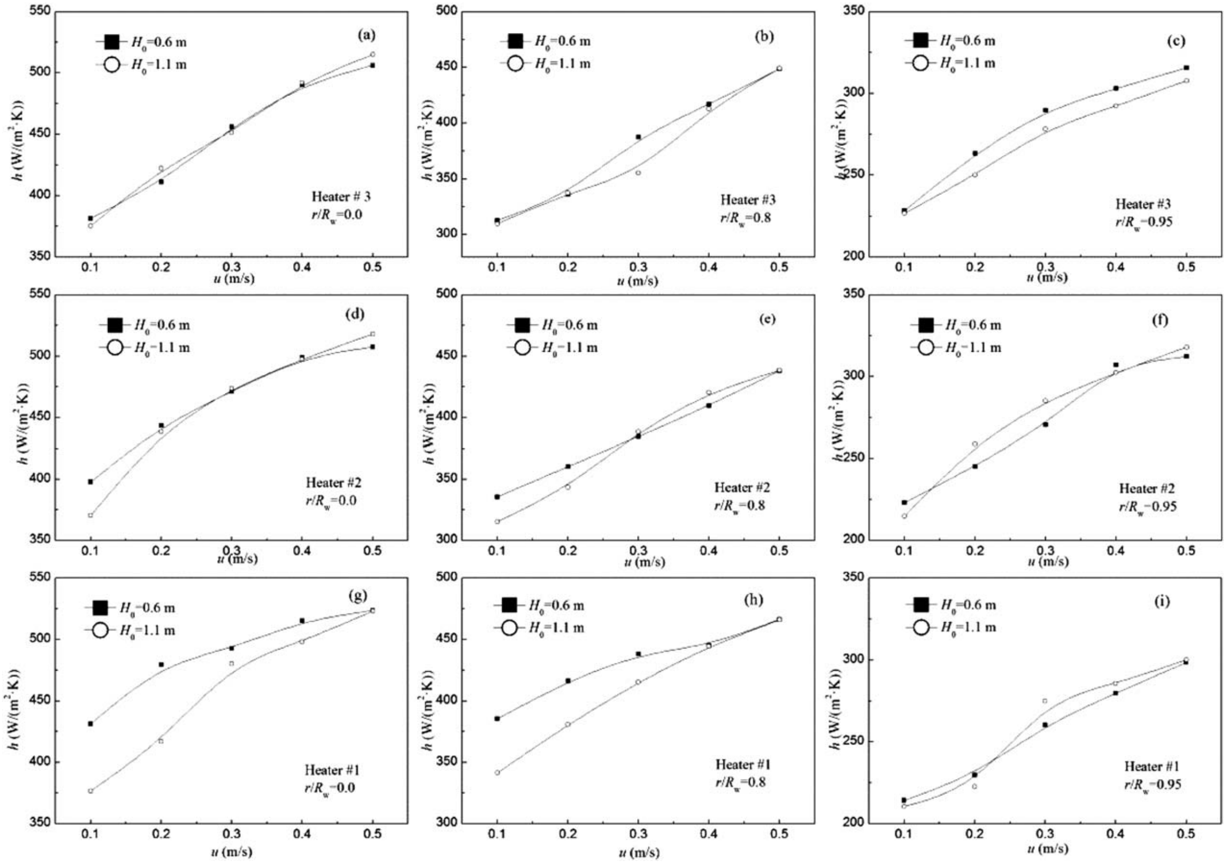

Figure 23. Effect of static bed height on heat-transfer coefficients.

$$C=\exp\left[\frac{-a_1}{Fo^{a_2+a_3\ln Fo}}\right]^{1/2} \tag{16}$$

where

$$Fo=\frac{k_{\mathrm{pa}}\tau_{\mathrm{pa}}}{c_{\mathrm{pa}}\rho_{\mathrm{p}}(1-\varepsilon_{\mathrm{mf}})d_{\mathrm{p}}^2} \tag{17}$$

$$a_1=0.213+0.117w+0.041w^2 \tag{18}$$

$$a_2=0.398-0.049w \tag{19}$$

$$a_3=0.022-0.003w \tag{20}$$

$$w=\ln\left(k_{\mathrm{pa}}/k_{\mathrm{g}}\right) \tag{21}$$

Figure 25 compares the experimental data and the predicted results by the models of Mickley and Fairbanks[24] and Chandran and Chen[37] using the determined packet fraction and mean packet residence time in this study. A detailed comparison of the models of Mickley and Fairbanks[24] and Chandran and Chen[37] used in this study is listed in Table 3. It is noted that only the expressions for k_{pa}, ρ_{pa} and C are different. As seen in Figure 25, both models successfully predict the right increasing trend of h with increasing superficial gas velocity. However, their predicted values of h are all below the corresponding experimental data. Comparatively, the Mickley and Fairbanks[24] model does a better job than the Chandran and Chen model.[37]

In a previous report, Chen[16] reported good agreement between their experimental and modeled results, but very large discrepancies are encountered in this study as shown in Figure 25. Why? A systematic survey of the modeling process can conclude that the critical voidage, which distinguishes packet and bubble phase, and $\varepsilon_{\mathrm{pa}}$, which determines ρ_{pa} and k_{pa}, should be the two key factors. In the study, we have calculated the solids volume fractions of packet at different superficial gas velocities and found they are almost constant, independent of superficial gas velocity and other hydrodynamic parameters in bed. The packet voidage determined in this study was only slightly smaller than the minimum fluidization voidage used by Chandran and Chen.[36] Figure 26 compares the predicted heat-transfer coefficients by the two methods listed in Table 3. It is seen there are only very small differences. Therefore, it can be concluded that the effect of $\varepsilon_{\mathrm{pa}}$ is less important.

Figure 27 shows the effect of the critical voltage (i.e., the critical voidage) on the predicted heat-transfer coefficients. At various locations and superficial gas velocities, the predicted heat-transfer coefficients are all found to increase with increasing critical voltage. As shown in Figure 9, increasing critical voltage leads to more bubble identified and thus higher packet renewal frequency, which is favorable to higher heat-transfer coefficient. In this study, we used a higher voltage, which corresponded to a lower voidage than Chandran and Chen.[31] This may explain the better performance of the Mickley and Fairbanks model[24] than the Chandran and Chen model.[37] Moreover, the selected critical voltage in this study may be still smaller than the actual value, which resulted in some small bubbles incapable of being identified and thus the underestimated packet renewal frequency. This may be cause why the predicted results of Mickley and Fairbanks model[24] are still small than experimental data. Finally, the good agreement between experimental and modeled results reported by Chen[16] was achieved on the basis of his specially selected critical voidage and a complex calculation method for the correction factor (Eqs. 16–21). Larger Geldart B particles were used in their study. The performances of their capacitance probe were also different from the optical fiber probe in this study. Therefore, it is not strange that the different modeling performance appears in this study. Strictly speaking, packet is more a modeling definition than a physical existence. The accurate determination of its physical properties may be impossible to be achieved. All the measurements methods, including in Chandran and Chen,[31] Kim et al.[30,32] and our study, more or less have their advantages and limitations.

In view of the difficulty to accurately determine the packet parameters, a correction factor was used in the Mickley and

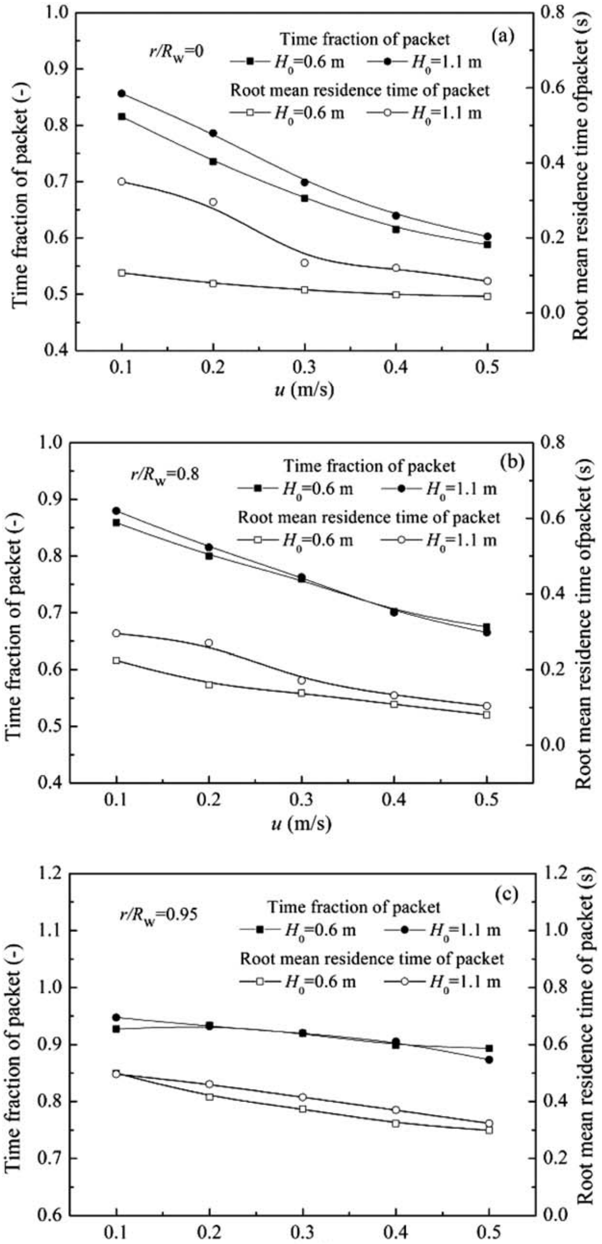

Figure 24. Effect of static bed height on tube surface hydrodynamic parameters (Heater #1).

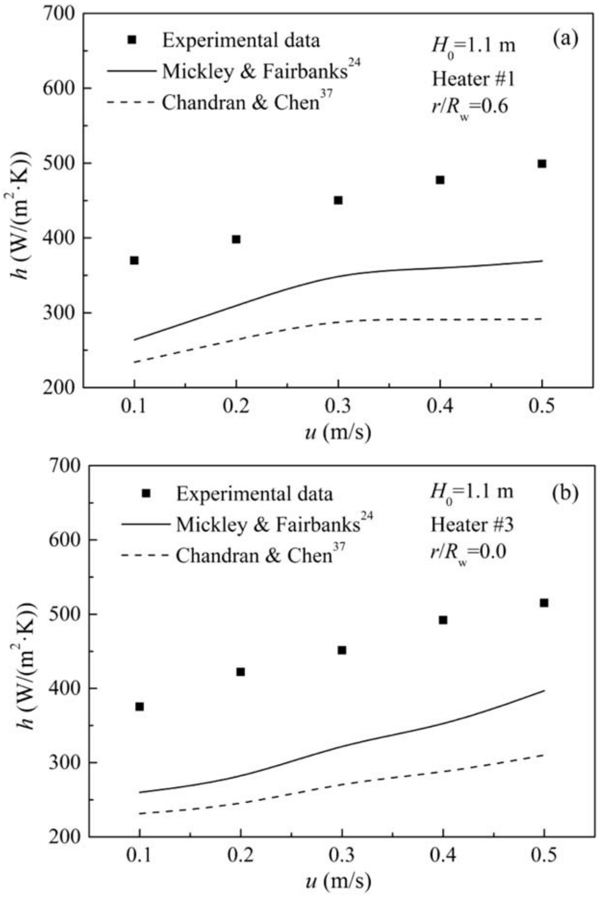

Figure 25. Comparison of the predicted heat-transfer coefficients by the models of Mickley and Fairbanks[24] and Chandran and Chen[36] and experimental data.

Table 3. Comparison of the Models of Chandran and Chen[37] and Mickley and Fairbanks[24]

	Chandran and Chen Model[37]	Mickley and Fairbank's Model[24]
h	$h=2C\delta_{\mathrm{pa}}\left[\frac{k_{\mathrm{pa}}\rho_{\mathrm{pa}}c_{\mathrm{pa}}}{\pi\tau_{\mathrm{pa}}}\right]^{1/2}$	
k_{pa}	$k_{\mathrm{pa}}=k_{\mathrm{g}}\left[\varepsilon_{\mathrm{mf}}+\frac{(1-\varepsilon_{\mathrm{mf}})}{\phi_{\mathrm{k}}+2k_{\mathrm{g}}/3k_{\mathrm{s}}}\right]$	$k_{\mathrm{pa}}=k_{\mathrm{g}}\left[\overline{\varepsilon_{\mathrm{pa,exp}}}+\frac{\left(1-\overline{\varepsilon_{\mathrm{pa,exp}}}\right)}{\phi_{\mathrm{k}}+2k_{\mathrm{g}}/3k_{\mathrm{s}}}\right]$
ρ_{pa}	$\rho_{\mathrm{pa}}=\rho_{\mathrm{p}}(1-\varepsilon_{\mathrm{mf}})$	$\rho_{\mathrm{pa}}=\rho_{\mathrm{p}}(1-\overline{\varepsilon_{\mathrm{pa,exp}}})$
c_{pa}	c_{ps}	
ϕ_{k}	$\phi_{\mathrm{k}}=0.305\left(\frac{k_s}{k_g}\right)^{-0.25}$ for $1\leq\frac{k_s}{k_g}\leq 1000$	
δ_{pa}	$\delta_{\mathrm{pa}}=\frac{\sum_{i=1}^{n}\tau_{\mathrm{pa,i}}}{t}$	
τ_{pa}	$\tau_{\mathrm{pa}}=\left[\frac{\sum_{i=1}^{n}\tau_{\mathrm{pa,i}}}{\sum_{i=1}^{n}\sqrt{\tau_{\mathrm{pa,i}}}}\right]^2$	
C	$C=\exp\left[\frac{-a_1}{Fo^{a_2+a_3\ln Fo}}\right]^{1/2}$ $Fo=\frac{k_{\mathrm{pa}}\tau_{\mathrm{pa}}}{c_{\mathrm{pa}}\rho_{\mathrm{p}}(1-\varepsilon_{\mathrm{mf}})d_{\mathrm{p}}^2}$ $a_1=0.213+0.117w+0.041w^2$ $a_2=0.398-0.049w$ $a_3=0.022-0.003w$ $w=\ln\left(k_{\mathrm{pa}}/k_{\mathrm{g}}\right)$	1

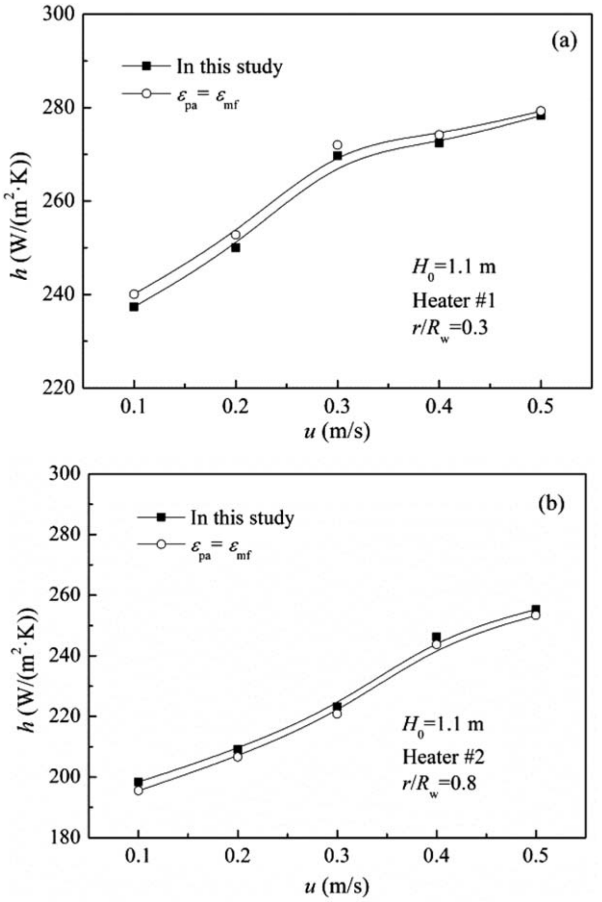

Figure 26. Effect of ε_{pa} on the predicted heat-transfer coefficients.

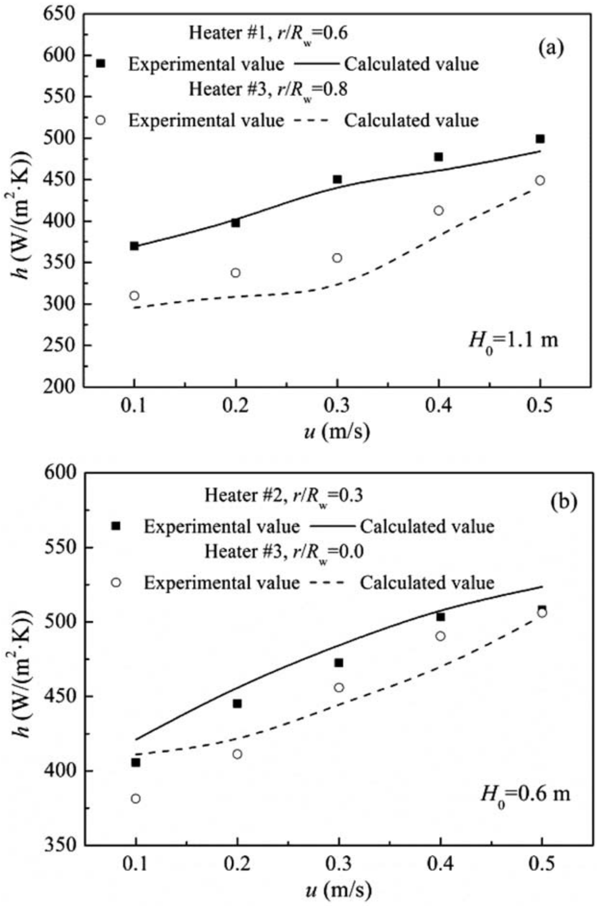

Figure 28. Comparison of the predicted heat-transfer coefficients by the modified Mickley and Fairbanks model and experimental data.

Fairbanks model, similar to the Chandran and Chen model,[37] to establish a more practical model to predict the heat-transfer coefficient. We found a constant of 1.3 was enough to achieve a satisfactory agreement between experimental data and the modeled results. Figure 28 shows the comparison between the modeled and experimental results at different positions. The agreements are found to be much better than in Figure 25. The range of the relative errors can be within −17%–30% as shown in Figure 29. The performance of several empirical models[20,39,40] are also compared with the modified Mickley amd Fairbanks model[24] with a correction factor and Chandran and Chen model[37] in Figure 30. It is seen that the packet renewal models perform much better than other empirical models. This is common that in fluidization research that extrapolation of existing empirical correlations can lead to unexpected large errors.

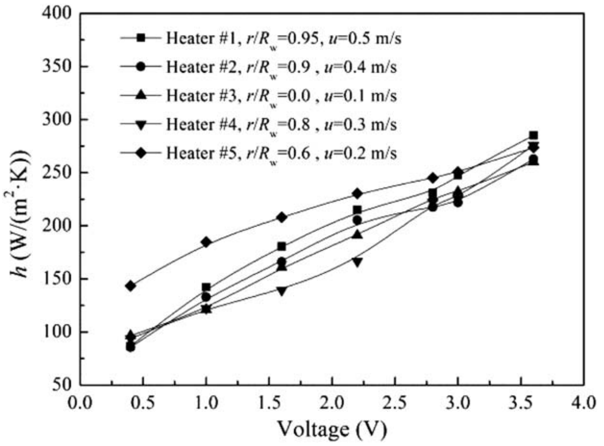

Figure 27. Effect of the critical voltage on the predicted heat-transfer coefficients.

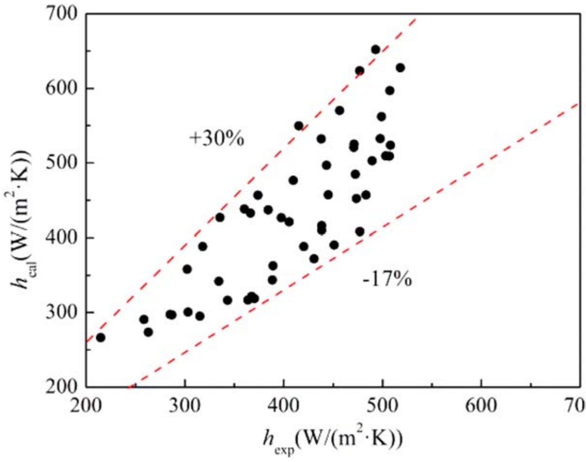

Figure 29. Relative errors between the modeled and experimental results.

[Color figure can be viewed in the online issue, which is available at wileyonlinelibrary.com.]

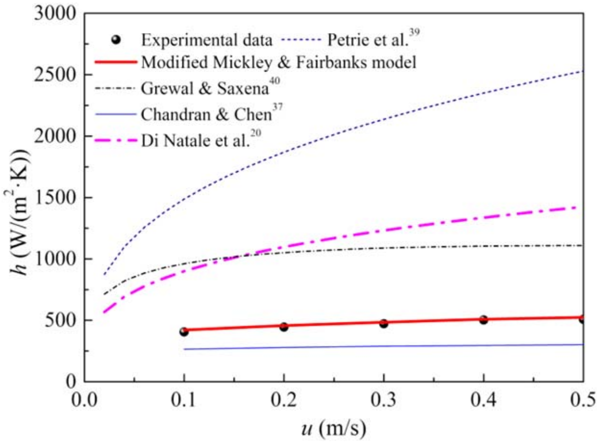

Figure 30. Comparison of the performance of different models.

[Color figure can be viewed in the online issue, which is available at wileyonlinelibrary.com.]

Conclusions

Through the aforementioned systematic study on the heat transfer properties and surface hydrodynamics of a vertical heat tube immersed in a fluidized bed of FCC particles, the following conclusions can be drawn:

1. Wall-to-bed heat-transfer coefficients at different axial and radial positions could be measured by the instrument developed in this study efficiently and with high accuracies. The measurement and data processing methods for tube surface hydrodynamics were also proved to be successful. The determined packet parameters could be used to explain a lot of important heat transfer properties.

2. At a given superficial gas velocity, the measured heat-transfer coefficients are high and constant in the center region ($r/R_w \leq 0.6$) and decrease with increasing speed as the heat tube approaches to the column wall. The measured radial profiles of mean packet residence time are found to be consistent to the radial changes of heat-transfer coefficient based on the packet renewal theory. Comparatively, the mean packet residence time, that is, an indicator of the packet renewal frequency, plays a more dominant role than packet fraction in bed-to-wall heat transfer.

3. In the operating gas velocity range of this study, the measured heat-transfer coefficients are found to increase with increasing superficial gas velocity, which is also corresponding to the decreased mean packet residence time measured by the optical fiber probe.

4. For the two investigated static bed heights of 0.6 and 1.1 m, higher heat-transfer coefficients are measured at $H_0 = 0.6$ m, which is more pronounced at lower superficial gas velocities. The measured mean packet residence times at the center of bed bottom at $H_0 = 0.6$ m are found to be higher than at $H_0 = 1.1$ m, which is believed to be the cause of the higher heat-transfer coefficients at $H_0 = 0.6$ m.

5. With a fitted correction factor, the modified Mickley and Fairbanks model is capable of predicting the quantitative value of heat-transfer coefficients successfully based on the determined packet parameters in this study. It is found that a proper selection of the critical voidage for distinguishing packet and bubble phase plays a critical role on the feasibility of the tube surface hydrodynamics measurement.

Acknowledgments

The authors acknowledge the financial supports by the National Natural Science Foundation of China (21276273), the Ministry of Science and Technology of China (2012CB215004 and 2012BAE05B02), the Ministry of Education of China by the Program for New Century Excellent Talents in University (NCET-11-0733), and the Science Foundation of China University of Petroleum, Beijing (KYJJ2012-03-11).

Notation

a_1, a_2, a_3 = model factors, dimensionless
A = cylindrical heat transfer area of a heat tube, m^2
$A_{2\text{-}3}$ = end heat transfer area between Heaters #3 and #2, m^2
A_3 = cylindrical heat transfer area of Heater #3, m^2
$A_{4\text{-}3}$ = end heat transfer area between Heaters #3 and #4, m^2
Ar = Archimedes number $(\rho_g(\rho_p-\rho_g)d_p^3 g/\mu^2)$, dimensionless
C = correction factor, dimensionless
c_{pa} = heat capacity of packet, J/kg
c_{pg} = heat capacity of gas, J/kg
c_{ps} = heat capacity of solid, J/kg
d_p = particle diameter, m
Fo = Fourier modulus, Eq. 17, dimensionless
h = bed-to-wall heat-transfer coefficient, W/(m^2·K)
$h_{2\text{-}3}$ = heat transfer coefficient between Heaters #3 and #2, W/(m^2 K)
h_3 = measured bed-to-wall heat-transfer coefficient of Heater #3, W/(m^2 K)
$h_{3\text{-}0}$ = real bed-to-wall heat-transfer coefficient of Heater #3, W/(m^2 K)
$h_{4\text{-}3}$ = heat-transfer coefficient between Heaters #4 and #2, W/(m^2 K)
h_g = gas convective heat-transfer coefficient, W/(m^2 K)
h_p = particle convective heat-transfer coefficient, W/(m^2 K)
h_{rad} = radiation heat-transfer coefficient, W/(m^2 K)
H_0 = static bed height, m
H_f = expanded bed height, m
g = gravitational acceleration, m/s^2
k_g = thermal conductivity of gas, W/(m·K)
k_{pa} = thermal conductivity of packet, W/(m·K)
k_s = thermal conductivity of solid, W/(m·K)
Nu_p = Nusselt number based on particle diameter (hd_p/k_g), dimensionless
p_A,p_B,p_C = gauge pressures measured at Taps A–C, Pa
Q_{in} = input power by the heating wire, W
Q_{out} = emiting heat flux, W
Q_{R1} = heat loss transferred from Heater #3 to Heater #4, W
Q_{R2} = heat loss transferred from Heater #3 to Heater #2, W
r = radial position, m
R = resistance of a heating wire, Ω
R_3 = resistance of the heating wire in Heater #3, Ω
Re = Reynolds number $(d_p\rho_g u/\mu)$, dimensionless
R_w = maximum radial position that the heater tube can reach, m
t = total sampling time, s
T_b = bed temperature, °C
T_w = heater wall temperature, °C
T_{w1}–T_{w5} = wall temperature of Heater #1–#5, °C
u = superficial gas velocity, m/s
U = voltage signal of the optical fiber probe, V
U_h = input voltage of a heating wire, V
U_{h3} = input voltage of the heating wire in Heater #3, V
w = $\ln(k_{pa}/k_g)$, dimensionless
z = distance from the distributor, m

Greek symbols

δ_{pa} = packet fraction, dimensionless
Δh = distance between the two taps of a differential pressure transducer, m
ε = voidage, dimensionless
ε_{mf} = voidage of minimum fluidization, dimensionless
ε_{pa} = packet voidage, dimensionless
$\overline{\varepsilon_{pa,exp}}$ = mean packet voidage determined by experiment, dimensionless
μ = gas viscosity, kg/(m s)

π = ratio of the circumference of a circle to its diameter, dimensionless
ρ_g = gas density, kg/m^3
ρ_p = particle density, kg/m^3
ρ_{pa} = packet density, kg/m^3
τ_{pa} = mean packet residence time, s
$\tau_{pa,i}$ = residence time of a packet, s
ϕ_w = 0.305 $(k_s/k_g)^{-0.25}$, dimensionless

Literature Cited

1. Davidson JF, Clift R, Harrison D. *Fluidization (2 ED)*. London, UK: Academic Press, 1985.
2. Kunii D, Levenspiel O. *Fluidization Engineering (2 ED)*. Butterworth-Heinemann, 1991.
3. Chan TY, Soni DS, Zhang F. Advances in a catalyst cooler technology. *Petrol Technol Q Autumn*. 1999;87:83–84.
4. Pillai R, Niccum PK. FCC catalyst coolers open window to increased propylene. *Proceeding of Grace Davison FCC Conference*, Munich, Germany, 2011.
5. Bai Y. Heat transfer in the circulating fluidized bed of a commercial catalyst cooler. *Powder Technol.* 2000;111(1–2):83–93.
6. Yang J. Cause analysis and measures for damage of tube and lining of external catalyst cooler in RFCC. *Petro-Chem Equip Technol.* 2009;30(1):35–38. (in Chinese)
7. Zhou H. Reason analysis and improvement of external heat-remover failure for catalyst cracker. *Petro-Chem Equip Technol.* 2001;22(2): 8–10. (in Chinese)
8. Zhang R, Zhang R. Development and application of a dense phase FCC catalyst cooler with enhanced heat-transfer capacity. *Pet Process Petrochem.* 2006;37(4):50–54. (in Chinese)
9. Wilson JW. *Fluid Catalytic Cracking Technology and Operations*. Tulsa: PennWell Publishing Company, 1997.
10. Lomas DA, Thompson GJ. Fluid particle cooling process and apparatus. *US Patent*, 4,434,245, 1984.
11. Zhang F, Li Z, Pi Y, Shi B. An external catalyst cooler with aeration controlled solids circulation. *Chinese Patent*, CN 1015901B, 1990. (in Chinese).
12. Chen J. *Catalytic Cracking Process and Engineering (2 ED)*. Beijing: China Petrochemical Press, 2005:1338–1343. (in Chinese)
13. Chen JC. Heat transfer in fluidized beds, Chapter 3. In Yang, WC, editor. *Fluidization, Solids Handling and Processing*, Noyes Publications, 1999:153–208.
14. Looi AY, Mao QM, Rhodes M. Experimental study of pressurized gas-fluidized bed heat transfer. *Int J Heat Mass Trans.* 2002;45(2): 255–265.
15. Ozkaynak TF, Chen JC, Frankenfield TR, An experimental investigation of radiant heat transfer in high temperature fluidized bed. In: *Fluidization IV*, New York: Engineering Foundation, 1983:371–378.
16. Chen JC. Surface contact-its significance for multiphase heat transfer: diverse examples. *J Heat Trans.* 2003;125:549–566.
17. Ozkaynak TF, Chen JC. Emulsion phase residence time and its use in heat transfer models in Fluidized Beds. *AIChE J.* 1980;26(4):544–550.
18. Abid BA, Ali JM, Alzubaidi AA. Heat transfer in gas-solid fluidized bed with various heater inclinations. *Int J Heat Mass Trans.* 2011; 54(9–10):2228–2233.
19. Lechner S, Merzsch M, Krautz HJ. Heat-transfer from horizontal tube bundles into fluidized beds with Geldart A lignite particles. *Powder Technol.* 2014;253:14–21.
20. Di Natale F, Lancia A, Nigro R. Surface-to-bed heat transfer in fluidised beds of fine particles. *Powder Technol.* 2009;195(2):135–142.
21. Stefanova A, Bi HT, Lim CJ, Grace JR. Heat transfer from immersed vertical tube in a fluidized bed of group A particles near the transition to the turbulent fluidization flow regime. *Int J Heat Mass Trans.* 2008;51(7–8):2020–2028.
22. Stefanova A, Bi HT, Lim CJ, Grace JR. Local hydrodynamics and heat transfer in fluidized beds of different diameter. *Powder Technol.* 2011;212(1):57–63.
23. Yao X, Sun F, Zhang Y, Lu C. Experimental validation of a new heat transfer intensification method for FCC external catalyst coolers. *Chem Eng Process.* 2014;75:19–30.
24. Mickley HS, Fairbanks DF. Mechanism of heat transfer to fluidized beds. *AIChE J.* 1955;1:374–384.
25. Mathur A, Saxena SC, Chao A. Heat transfer from an immersed vertical tube in a gas-fluidized bed. *Ind Eng Chem Process Des Dev.* 1986;25(1):156–163.
26. Di Natale F, Lancia A, Roberto N. Surface-to-bed heat transfer in fluidised beds: effect of surface shape. *Powder Technol.* 2007; 174(3):75–81.
27. Botterill JSM, Teoman Y, Yeregir KR. Factors affecting heat transfer between gas-fluidized beds and immersed surfaces. *Powder Technol.* 1984;39:177–189.
28. White TR, Mathur A, Saxena SC. Effect of vertical boiler tube diameter on heat transfer coefficient in gas-fluidized beds. *Chem Eng J.* 1986;32:1–13.
29. Vreedenberg HA. Heat transfer between a fluidized bed and a horizontal tube. *Chem Eng Sci.* 1958;9(1):52–60.
30. Kim SW, Ahn JY, Kim SD, Lee DH. Heat transfer and bubble characteristics in a fluidized bed with immersed horizontal tube bundle. *Int J Heat Mass Trans.* 2003;46(3):399–409.
31. Chandran R, Chen JC. Bed-surface contact dynamics for horizontal tubes in fluidized beds. *AIChE J.* 1982;29(6):907–913.
32. Kim SW, Namkung W, Kim SD. Solids behavior in freeboard of FCC regenerator. *J Chem Eng Jpn.* 2000;33(1): 78–85.
33. Li X, Yang C, Yang S, Li G. Fiber-optical sensors: basics and applications in multiphase reactors. *Sensors.* 2012;12(9):12519–12544.
34. Zhang H, Johnston PM, Zhu JX, de Lasa HI, Bergougnou MA. A novel calibration procedure for a fibre optic concentration probe. *Powder Technol.* 1998;100:266–272.
35. Pisters K, Prakash A. Investigations of axial and radial variations of heat transfer coefficient in bubbling fluidized bed with fast response probe. *Powder Technol.* 2011;207(1–3):224–231.
36. Chen JC, Grace JR, Golriz MR. Heat transfer in fluidized beds: design methods. *Powder Technol.* 2005;150(2):123–132.
37. Chandran R, Chen JC. A heat transfer model for tubes immersed in gas fluidized beds. *AIChE J.* 1985;31(2):244–252.
38. Kunii D, Smith JM. Heat transfer characteristics of porous rocks. *AIChE J.* 1960;1:71–78.
39. Petrie JC, Freeby WA, Buckham JA. In-bed heat exchanger. *Chem Eng Prog Symp Ser.* 1968;64:45–51.
40. Grewal NS, Saxena SC. Heat transfer between a horizontal tube and a gas-solid fluidized bed. *Int J Heat Mass Trans.* 1980;23(11):1505–1519.

Manuscript received Apr. 3, 2014, and revision received Aug. 16, 2014.